

Near-field radiative heat transfer between nonpolar epsilon-near-zero dielectric-filled Si gratingsGui-Cheng Cui,^{1,2} Cheng-Long Zhou,^{1,2,3} Yong Zhang,^{1,2} and Hong-Liang Yi^{1,2,*}¹*School of Energy Science and Engineering, Harbin Institute of Technology, Harbin 150001, People's Republic of China*²*Key Laboratory of Aerospace Thermophysics, Ministry of Industry and Information Technology, Harbin 150001, People's Republic of China*³*Department of Electrical and Computer Engineering, National University of Singapore, Singapore 117583, Singapore*

(Received 11 December 2023; revised 3 March 2024; accepted 11 March 2024; published 27 March 2024)

Epsilon-near-zero (ENZ) materials have attracted significant attention in the far- and near fields of thermal radiation in recent years because of their unique optical characteristics. However, it is not considered an optimal carrier for near-field radiative heat transfer (NFRHT) due to the excessively low frustrated mode. In this paper, we address this drawback with a metamaterial composed of artificial hypothetical nonpolar ENZ dielectric-filled Si gratings. The behavior of NFRHT with ENZ has been investigated based on fluctuational electrodynamic and rigorous coupled-wave analysis. An artificial mode named Meta-NP ENZ mode is presented to reveal the significant enhancement of NFRHT, which can be demonstrated by the electric field intensity enhancement. Furthermore, we find that the increasing imaginary part may lead to an anomalous amplification of heat flux despite causing a recession in the Meta-NP ENZ mode, and this mode remains robust with respect to the plasma frequency shift of grating material. Our findings demonstrate that the ENZ dielectric exhibits outstanding performances similar to those observed in far-field radiation, surpassing the limitations of both Si gratings and nonpolar ENZ dielectric in NFRHT.

DOI: [10.1103/PhysRevB.109.125430](https://doi.org/10.1103/PhysRevB.109.125430)**I. INTRODUCTION**

Epsilon-near-zero (ENZ) materials have attracted a great deal of attention in the field of radiation due to their unique optical properties. Under far-field radiation conditions, as the electromagnetic wave propagates in ENZ dielectric with a permittivity approaching zero, the wavelength is stretched. The strong field confinement can be maintained in subwavelength dimensions. This leads to enhanced absorption for highly directional emission, nonlinearity enhancement, and others [1–4]. However, as the distance between two objects is close to or less than the characteristic wavelength of thermal radiation, these prominent effects disappear, because in the near-field scenarios, the main carriers of energy transmission are evanescent waves rather than propagation waves. When there are no surface modes, the flux for evanescent waves comes from the frustrated mode contribution only. As the permittivity is less than 1, frustrated modes cannot exist. In other words, the nonpolar ENZ dielectric cannot facilitate photon tunneling under large wave vectors and thus cannot exhibit strong enhancement on near-field radiative heat transfer (NFRHT), which can exceed the blackbody limit by several orders of magnitude [5–8].

This phenomenon contradicts the nonlinear enhancement observed in far-field radiation within ultrathin ENZ medium, posing a challenge for the application of nonpolar ENZ materials in NFRHT. Currently, it has been observed that polar material with a permittivity less than zero exhibits enhanced

support for evanescent waves due to its near-zero property. However, nonpolar material with a permittivity greater than zero seems to encounter a forbidden zone in terms of NFRHT when it comes to the near-zero property. Although a remarkable enhancement of NFRHT can be achieved due to the epsilon-near-zero feature exhibited by hyperbolic materials [9,10], natural materials manifest zero-crossing points for the real part of the permittivity near-plasma or interband transition frequencies which is typically observed within a narrow band. The open question of whether nonpolar ENZ materials can be made to function as magically for near-field radiative heat transfer as they do for far-field radiation remains unanswered. Thus, we employ a metamaterial to overcome this limitation. Metamaterials are periodic artificial arrays composed of subwavelength structures that exhibit extraordinary physical properties not present in natural materials. They have solved some insurmountable problems in the fields of optics and acoustics such as perfect lenses [11,12], invisibility cloaks [13–15], and sound attenuation [16–18]. This is attributed to the perfect wave-absorbing properties. On the other hand, the prominent contributions of metamaterials in improving NFRHT by hybridizing various modes or polaritons have also received attention [19–25].

Inspired by artificial metamaterials, we construct a metamaterial composed of Si gratings filled with an artificial hypothetical nonpolar ENZ dielectric, characterized by a constant permittivity. We investigate the impact of near-zero values in real and imaginary parts of permittivity on NFRHT, respectively. Our main focus is on calculating the energy transmission coefficients and evaluating the near-field radiative heat flux. Ultimately, our findings demonstrate that the

*yihongliang@hit.edu.cn

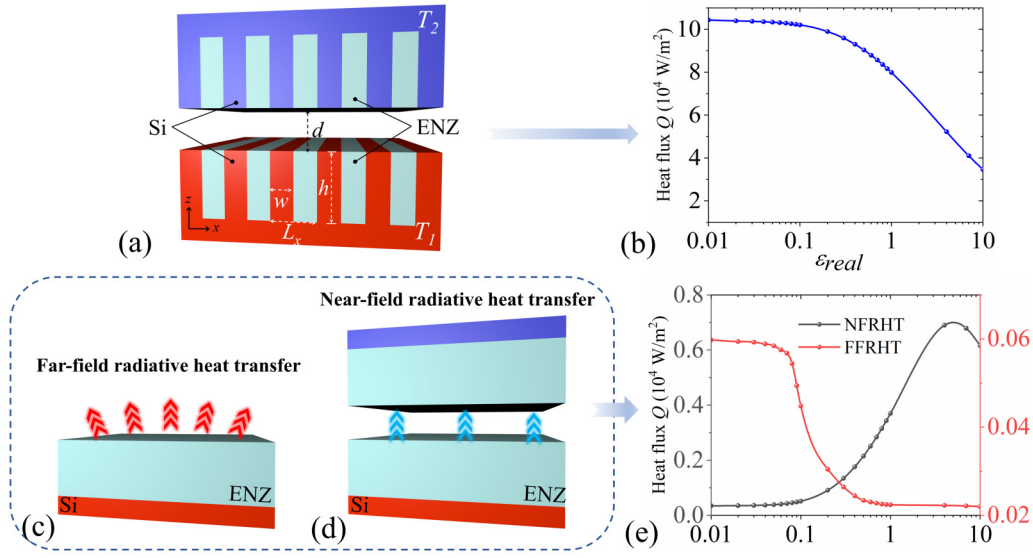


FIG. 1. (a) Schematic of nonpolar ENZ-filled doped Si gratings. (b) Total heat flux of metamaterial. (c) Far-field radiative heat transfer (FFRHT) of Si substrate covered with Si plate. (d) Near-field radiative heat transfer (NFRHT) of Si substrate covered with ENZ plate. (e) Total heat flux of FFRHT and NFRHT.

extraordinary optical properties of nonpolar ENZ dielectric paradoxically enhance NFRHT by facilitating a unique ENZ mode that surprisingly couples surface plasmon polaritons (SPPs) and magnetic polaritons (MPs) inherent in metamaterials. The significance of confined MPs in grating grooves as dominant polaritons in NFRHT requires further discussion, while the LC circuits fail to accurately predict the resonance frequency under ENZ conditions. In addition, we investigate the loss of nonpolar ENZ dielectric and find that the imaginary part near zero cannot induce the maximum heat flux as the real part does. Finally, we validate the robustness of this metamaterial with respect to variations in metal plasma frequency, which exhibits a more universal behavior. This discovery breaks the limitations of nonpolar ENZ materials in NFRHT and achieves a comparable enhancement effect to that observed in far-field radiation.

II. METHOD

The near-field radiative heat transfer of two parallel metamaterials is illustrated in Fig. 1(a). For one-dimensional gratings, we set the initial geometrical parameters (period, ridge width, height, vacuum gap) as $L_x = 100$ nm, $w = 50$ nm, $h = 300$ nm, and $d = 60$ nm. The temperatures of emitter and receiver are expressed as $T_1 = 400$ K and $T_2 = 300$ K, respectively. Based on the scattering theory, the near-field radiative heat transfer between two periodic gratings is given by [26,27]

$$Q_{\text{exact}} = \frac{1}{8\pi^3} \int_{-\infty}^{+\infty} \int_{-\pi/L_x}^{+\pi/L_x} \int_0^{+\infty} [\Theta(T_1, \omega) - \Theta(T_2, \omega)] \times \xi(\omega, k_x, k_y) d\omega dk_x dk_y, \quad (1)$$

$$\Theta(T, \omega) = \frac{\hbar\omega}{\exp[\hbar\omega/k_B T] - 1}, \quad (2)$$

where $\Theta(T, \omega)$ denotes the mean energy of thermal harmonic oscillators where k_x and k_y are x and y components of wave vector k , respectively. Due to the periodicity in the x direction, k_x is restricted to the first Brillouin zone, i.e., $-\pi/L_x < k_x < +\pi/L_x$, while k_y is not bound by any restrictions, i.e., $-\infty < k_y < +\infty$. And, the energy transmission coefficient $\xi(\omega, k_x, k_y)$ is expressed as [28,29]

$$\xi(\omega, k_x, k_y) = \text{Tr}(\mathbf{D}\mathbf{W}_1\mathbf{D}^\dagger\mathbf{W}_2), \quad (3)$$

$$\mathbf{D} = (\mathbf{I} - \mathbf{S}_1\mathbf{S}_2)^{-1}, \quad (4)$$

$$\mathbf{W}_1 = \sum_{-1}^{pw} -\mathbf{S}_1 \sum_{-1}^{pw} \mathbf{S}_1^\dagger + \mathbf{S}_1 \sum_{-1}^{ew} - \sum_{-1}^{ew} \mathbf{S}_1^\dagger, \quad (5)$$

$$\mathbf{W}_2 = \sum_1^{pw} -\mathbf{S}_2^\dagger \sum_1^{pw} \mathbf{S}_2 + \mathbf{S}_2^\dagger \sum_1^{ew} - \sum_1^{ew} \mathbf{S}_2, \quad (6)$$

where Tr means the trace of a matrix, \mathbf{D} is the inverse of a Fabry-Perot-like factor, $\mathbf{S}_1 = \mathbf{R}_1$, and $\mathbf{S}_2 = \exp(ik_{z_0}d) \cdot \mathbf{R}_2 \cdot \exp(ik_{z_0}d)$. The projectors on the propagative and evanescent waves are expressed as $\sum_{1(-1)}^{pw(ew)} = 0.5k_{z_0}^{1(-1)} \prod_{pw(ew)}$, where k_{z_0} is the vertical component of the wave vector in vacuum, and $\prod_{pw(ew)}$ are expressed as

$$\prod_{\alpha\alpha'}^{pw} = \delta_{\alpha\alpha'} [1 + \text{sgn}(k_0^2 - k_{x,y}^2)], \quad (7a)$$

$$\prod_{\alpha\alpha'}^{ew} = \delta_{\alpha\alpha'} [1 - \text{sgn}(k_0^2 - k_{x,y}^2)], \quad (7b)$$

where $\delta_{\alpha\alpha'}$ is the Kronecker operator, and $\mathbf{k}_{x,y} = [k_x + (2\pi n/L_x)\hat{x} + k_y\hat{y}]$ is the total lateral wave vector. Note that \mathbf{R}_1 and \mathbf{R}_2 represent the reflection matrices of objects 1 and 2 calculated by using the rigorous coupled-wave analysis (RCWA) method, respectively. They both are $2(2N + 1)$ dimensions, where N is the truncated diffraction order [30,31]. The p - and s modes are calculated in \mathbf{R} , which

is determined by

$$\mathbf{R} = \begin{bmatrix} \mathbf{R}_{-N,N}^{PP} & \mathbf{R}_{-N,N}^{PS} \\ \mathbf{R}_{-N,N}^{SP} & \mathbf{R}_{-N,N}^{SS} \end{bmatrix}. \quad (8)$$

According to the RCWA, the grating region is a periodic structure composed of alternating Si and ENZ material. To solve the reflection matrix, the Fourier expansion of permittivity of the materials in the grating region is expressed as

$$\varepsilon(x) = \sum_N e_N e^{j(2\pi/L_x)Nx}, \quad (9)$$

$$\frac{1}{\varepsilon(x)} = \sum_N \tilde{e}_N e^{j(2\pi/L_x)Nx}, \quad (10)$$

$$e_N = \begin{cases} (\varepsilon_{\text{Si}} - \varepsilon_{\text{ENZ}})(x_2 - x_1) + \varepsilon_{\text{ENZ}}, & N = 0 \\ \frac{j(\varepsilon_{\text{Si}} - \varepsilon_{\text{ENZ}})}{2\pi N} [e^{-j2\pi Nx_2} - e^{-j2\pi Nx_1}], & N \neq 0 \end{cases}, \quad (11)$$

$$\tilde{e}_N = \begin{cases} \left(\frac{1}{\varepsilon_{\text{Si}}} - \frac{1}{\varepsilon_{\text{ENZ}}}\right)(x_2 - x_1) + \frac{1}{\varepsilon_{\text{ENZ}}}, & N = 0 \\ \frac{j\left(\frac{1}{\varepsilon_{\text{Si}}} - \frac{1}{\varepsilon_{\text{ENZ}}}\right)}{2\pi N} [e^{-j2\pi Nx_2} - e^{-j2\pi Nx_1}], & N \neq 0 \end{cases}, \quad (12)$$

where x_2 and x_1 represent the relative position coordinates of Si grating in one period, respectively, and the difference between the two can be used to determine the filling ratio of Si grating. The range from $-N$ to N means the order of Brillouin zones. To ensure the accuracy of the results and to minimize the calculation time, N is set as 101 to achieve rapid convergence of the calculation results. As for doped Si, the permittivity is attained by [32]: $\varepsilon_{\text{Si}} = 11.7 - \omega_p^2/(\omega^2 + i\gamma\omega)$, where ω_p and γ are taken as 1.08×10^{15} and 9.35×10^{13} rad/s, respectively.

On the other hand, the nonpolar epsilon-near-zero dielectric can be regarded as an ideal material and its permittivity is artificially given by $\varepsilon_{\text{ENZ}} = \varepsilon_{\text{real}} + i\varepsilon_{\text{imag}}$. In our work, we do not consider the dispersion characteristics of permittivity with frequency, and thus both real and imaginary parts are set as constants.

III. RESULTS AND DISCUSSION

Current research has demonstrated that the giant field intensity enhancement generated in dielectric can improve the light-matter interactions due to the presence of ENZ mode and enhance the absorption of electromagnetic waves in far-field radiation [33]. However, nonpolar ENZ dielectric cannot facilitate the transmission of large wave-vector evanescent waves in NFRHT, leading to a lower radiative heat flux compared to that with high permittivity. Specifically, the contribution of evanescent waves to the radiative heat flux for plates can be calculated as follows:

$$\begin{aligned} q^{\text{evan}}(\omega) &= q^{\text{surface}} + q^{\text{frustrated}} \\ &= \frac{1}{\pi^2} \Theta(T, \omega) \int_{k_{\parallel}=k_0}^{\infty} k_{\parallel} e^{-2d\text{Im}(k_{\perp})} \\ &\quad \times \sum_{i=\text{TE, TM}} \frac{\text{Im}(r_{21}^i) \text{Im}(r_{23}^i)}{|1 - r_{21}^i r_{23}^i e^{2ik_{\perp}d}|^2} dk_{\parallel}. \end{aligned} \quad (13)$$

The frustrated-mode contribution $q^{\text{frustrated}}$ is calculated by integrating Eq. (13) on the k_{\parallel} from k_0 to $\sqrt{\varepsilon}k_0$, while the

surface-mode contribution q^{surface} results from the integration from $\sqrt{\varepsilon}k_0$ to ∞ . If ε is less than 1, frustrated modes cannot exist. In the absence of surface modes, the disappearance of frustrated modes must result in the evanescent-wave heat flux being zero. Nevertheless, when Si gratings are filled with nonpolar ENZ dielectric, the heat flux reaches its maximum value at $\varepsilon_{\text{real}}$ near zero, as shown in Figs. 1(c) and 1(e). This phenomenon has reignited our interest in comprehending the behavior of nonpolar ENZ dielectric in NFRHT.

We initially compare the radiative heat flux between meta-materials, gratings, and plates as depicted in Fig. 2. Both ENZ plate and ENZ gratings fail to surpass the limitation of blackbody radiation even at near-field distances, indicating that evanescent waves are not present. When replacing the nonpolar ENZ dielectric with Si, a significant enhancement in NFRHT is observed. The radiative heat flux reaches its peak near 2.9×10^{14} rad/s due to the SPPs supported by Si material. In contrast, Si gratings exhibit superior performance compared to Si plates. In addition to SPPs, unique MPs found in gratings are essential for improving NFRHT in the low-frequency range, as will be further discussed in subsequent sections. However, when filling Si gratings with nonpolar ENZ dielectric, the heat flux exceeds its limitation and reaches a peak at 2.25×10^{14} rad/s. In other words, nonpolar ENZ dielectric considerably enhances the performance of Si gratings and modifies the inherent spectral characteristics, even if it does not actively engage in NFRHT. Such a filled structure exhibits remarkable distinctions from heterostructures composed of gratings and two-dimensional materials like graphene or black phosphorus [8,34]. Two-dimensional materials can support SPPs that provide more surface modes for heterostructures, contributing more to radiative heat flux in different frequency bands. In contrast, nonpolar ENZ dielectric plate apparently fails to support surface modes, which raises questions about its diametrically opposite effect in Si gratings' behavior. Therefore, we will conduct an extensive investigation into how nonpolar ENZ dielectric affects NFRHT in Si gratings.

In order to demonstrate the crucial role of nonpolar ENZ dielectric in enhancing the NFRHT between Si gratings, we initially discuss the impact of $\varepsilon_{\text{real}}$. Thus, we select eight values of $\varepsilon_{\text{real}}$ ranging from 0.01 to 10 and calculate the energy transmission coefficients according to Eq. (3), as depicted in Fig. 3. Subsequently, we will elucidate three scenarios. When $\varepsilon_{\text{real}}$ is equal to 1, the filled medium can be regarded as a vacuum, i.e., the simple Si gratings in Fig. 3(e). Due to the strong resonance at around 1.5×10^{14} rad/s caused by magnetic polaritons induced by Si gratings, ξ extends to about $0.3k_x$ with the value close to 1 in the frequency range of $1.0\text{--}2.0 \times 10^{14}$ rad/s. This resonant mode provides an additional channel for photon tunneling and facilitates the transmission of evanescent waves [34,35]. On the other hand, surface plasmon polaritons represent another mode where the energy transmission coefficients similarly extend to $0.3k_x$ within the frequency range of $2.5\text{--}3.1 \times 10^{14}$ rad/s. It is not the same as MPs in that its maximum value is limited at 0.5. In other words, MPs exhibit stronger support for photon tunneling compared with SPPs in Si gratings. When $\varepsilon_{\text{real}}$ is greater than 1, the Si gratings are filled by nonpolar dielectric,

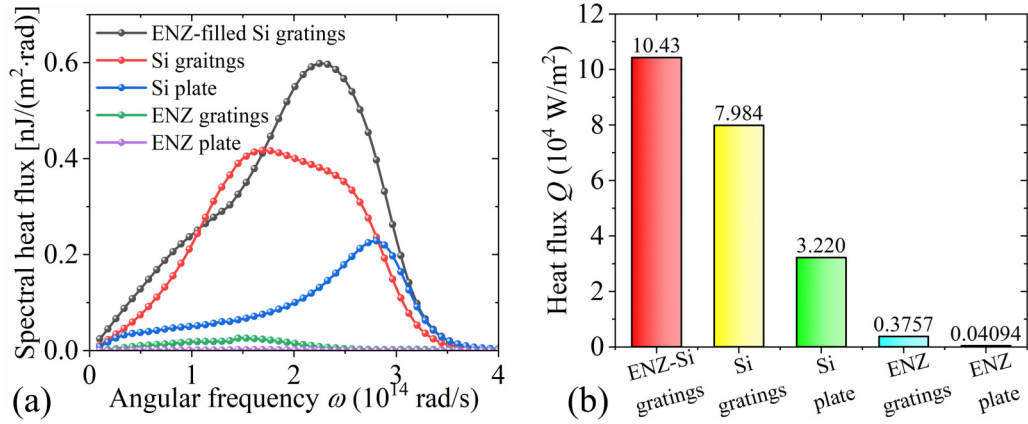


FIG. 2. (a) Spectral heat fluxes of ENZ-Si gratings, Si gratings, Si plate, ENZ gratings, and ENZ plate. The vacuum gap d of all scenarios is 60 nm. The temperatures of emitter and receiver are 400 and 300 K respectively. The permittivity of nonpolar ENZ material is $\epsilon = 0.01 + 0.0001i$. (b) Total heat fluxes of ENZ-Si gratings, Si gratings, Si plate, ENZ gratings, and ENZ plate.

as shown in Figs. 3(f)–3(h). Photon tunneling dominated by MPs shows a notable peak shift towards lower frequencies and cannot occur under large wave vectors as ϵ_{real} increases. Note that this frequency shift characteristic can be predicted by LC circuits, which will be analyzed below [36,37]. In contrast, the spectrum broadens when the energy transmission coefficients represented by SPPs approach 1 and grow in value. This is because filling the dielectric is equivalent to augmenting both the depth and width of grooves, resulting in more dispersive SPPs [25].

When ϵ_{real} is less than 1, it can be considered as the range where epsilon is near zero. As ϵ_{real} is equal to 0.01, the energy transmission coefficients extend to $0.7k_x$ wave vector near 2.1×10^{14} rad/s with a value exceeding 0.8, as depicted in Fig. 3(a). In this case, ξ does not exhibit a distinct distribution characterized by MPs or SPPs like in the vacuum-filled case.

Instead, a stronger and more homogeneous mode is formed which is referred to Meta-NP ENZ mode. This mode not only enhances the MPs and SPPs but also effectively couples the two polaritons in metamaterials, leading to potential radiative enhancement. As ϵ_{real} increases from 0.1 to 1, the Meta-NP ENZ mode splits and decouples into MPs and SPPs towards lower and higher frequencies, respectively, accompanied by ξ attenuating towards smaller wave vectors, as shown in Figs. 3(b)–3(e). Hence, we have identified the range of ϵ_{real} from 0.1 to 1 as the transition state, and this intriguing phenomenon can reveal the formation process of Meta-NP ENZ mode.

To investigate the dispersion properties of Meta-NP ENZ mode, we approximate the grating structure filled with ENZ dielectric as a homogeneous anisotropic plate based on the effective medium theory (EMT) [38,39]. The permittivity of

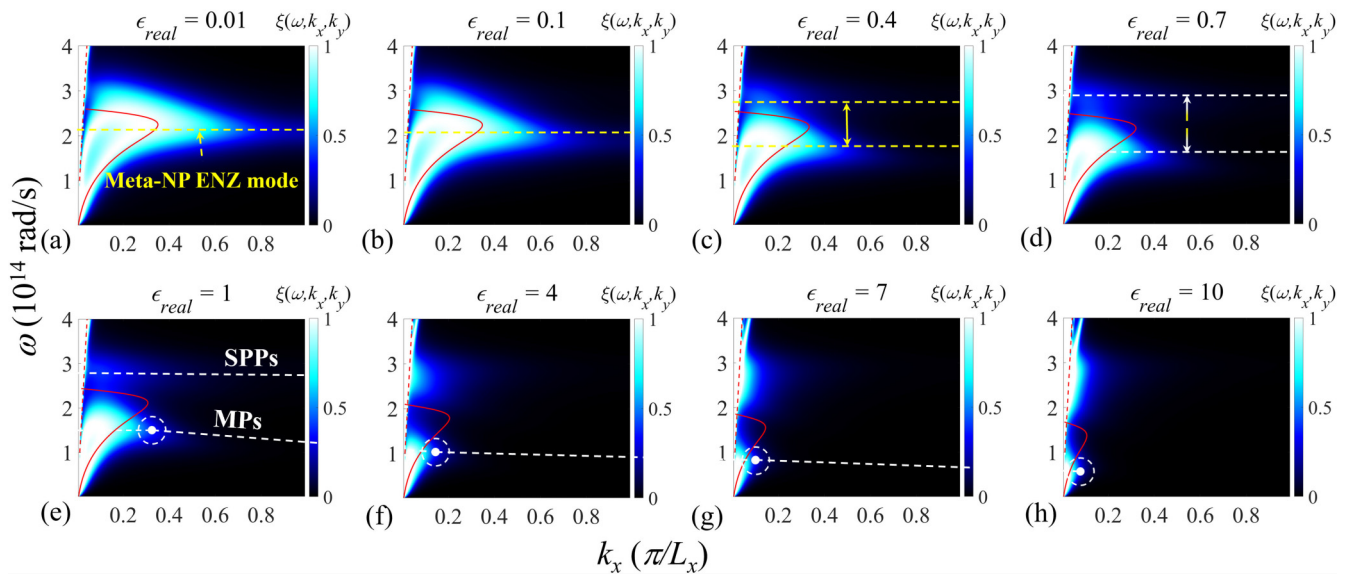


FIG. 3. Contour plots of energy transmission coefficients ξ of different ϵ_{real} within the first Brillouin zone at $k_y = 0$, and the imaginary part is fixed as 0.0001. (a) $\epsilon_{\text{real}} = 0.01$, (b) $\epsilon_{\text{real}} = 0.1$, (c) $\epsilon_{\text{real}} = 0.4$, (d) $\epsilon_{\text{real}} = 0.7$, (e) $\epsilon_{\text{real}} = 1$, (f) $\epsilon_{\text{real}} = 4$, (g) $\epsilon_{\text{real}} = 7$, and (h) $\epsilon_{\text{real}} = 10$. The dispersion properties calculated by EMT are plotted as the red solid lines. The white dots surrounded by the dashed white circles in (e)–(h) represent the MPs' frequencies at the maximum wave vectors where ξ exceeds 0.8.

this homogeneous material can be regarded as a uniaxial anisotropic material with an optical axis in the x direction, and its permittivity tensor is expressed as

$$\boldsymbol{\varepsilon} = \begin{bmatrix} \varepsilon_{xx} & 0 & 0 \\ 0 & \varepsilon_{yy} & 0 \\ 0 & 0 & \varepsilon_{zz} \end{bmatrix}, \quad (14)$$

$$\varepsilon_{xx} = \left(\frac{1 - f_{\text{Si}}}{\varepsilon_{\text{ENZ}}} + \frac{f_{\text{Si}}}{\varepsilon_{\text{Si}}} \right)^{-1}, \quad (15)$$

$$\varepsilon_{yy} = \varepsilon_{zz} = (1 - f_{\text{Si}})\varepsilon_{\text{ENZ}} + f_{\text{Si}}\varepsilon_{\text{Si}}, \quad (16)$$

where f is the filling ratio. In this case, the energy transmission coefficient $\xi_j(\omega, k_{xy})$ is given by [40,41]

$$\xi_j(\omega, k_{xy}) = \begin{cases} \frac{(1 - |r_{j,E}|^2)(1 - |r_{j,R}|^2)}{|1 - r_{j,E}r_{j,R}e^{2ik_0d}|^2}, & k_{xy} < k_0 \\ \frac{4\text{Im}(r_{j,E})\text{Im}(r_{j,R})e^{-2|k_0|d}}{|1 - r_{j,E}r_{j,R}e^{2ik_0d}|^2}, & k_{xy} > k_0 \end{cases}, \quad (17)$$

where $r_{j,E}$ and $r_{j,R}$ indicate the Fresnel reflection coefficients of the emitter and receiver, respectively. $k_0 = \omega/c_0$ means the magnitude of the wave vector, and $k_{z0} = (k_0^2 - k_{xy}^2)^{1/2}$ denotes the z component of the wave vector in vacuum. To obtain the asymptotic analysis of the near-field dispersion relation, the radiative heat flux diverges when the denominator in $\xi_j(\omega, k_{xy})$ fulfills the following condition:

$$1 - r_{j,E}r_{j,R}e^{2ik_0d} = 0. \quad (18)$$

In terms of a surface wave with $k_{xy} \gg k_0$, the z component of the wave vector can be estimated by $k_z = \sqrt{\varepsilon_{xx}k_0^2 - \varepsilon_{zz}k_{xy}^2} \approx i\sqrt{\frac{\varepsilon_{xx}}{\varepsilon_{zz}}}k_{xy} = \psi k_{xy}$, which enables us to further simplify the solution of Eq. (18). The allowable value of momentum k_z obeys the Fabry-Perot condition, and the frequency-resonant mode of ENZ-filled Si gratings can be expressed by invoking the quasistatic approximation [42,43]:

$$k_{xy}(\omega) = -\frac{1}{\psi h} \left[m\pi + 2 \arctan \left(\frac{\psi}{\varepsilon_{zz}} \right) \right], \quad (19)$$

where integer $m = 0$ denotes the resonance order. The dispersion properties are obtained by substituting different values of $\varepsilon_{\text{real}}$ into Eq. (19), as shown in red solid curves. When $\varepsilon_{\text{real}}$ is set to 0.01 and 0.1, the two curves exhibit considerable similarity at resonance frequency 2.16×10^{14} rad/s, and they coincide well with the highlighted region of energy transmission coefficients. This observation indicates that the EMT method accurately predicts the Meta-NP ENZ mode dispersion characteristics at $\varepsilon_{\text{real}}$ below 0.1.

However, when $\varepsilon_{\text{real}}$ is above 0.7, the resonance frequencies calculated by EMT exhibit a higher magnitude compared to those obtained by RCWA. This means that the dispersion curves no longer align with the distribution of energy transmission coefficients. As ε_{ENZ} approaches zero, ε_{xx} also tends to approach zero and the effect of ε_{Si} can be neglected. But, ε_{yy} and ε_{zz} can be approximated as $f_{\text{Si}} \varepsilon_{\text{Si}}$. This implies that the Meta-NP ENZ mode is formed when ε_{ENZ} is much smaller than ε_{Si} and remains robust within an $\varepsilon_{\text{real}}$ range between 0.01 and 0.1. However, once $\varepsilon_{\text{real}}$ increases beyond this range, it

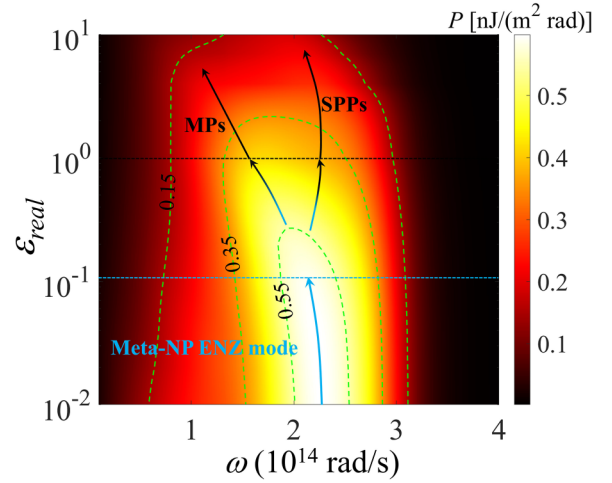


FIG. 4. Contour plot of spectral heat flux as a function of $\varepsilon_{\text{real}}$. The $\varepsilon_{\text{real}}$ range of Meta-NP ENZ mode is from 0.01 to 0.1. And, the $\varepsilon_{\text{real}}$ range of 0.1 to 1 is the transition state where the Meta-NP ENZ mode gradually decouples into MPs and SPPs.

leads to significant deviation in solving Eq. (19), since both ε_{xx} and ε_{zz} cannot be approximated as zero and $f_{\text{Si}} \varepsilon_{\text{Si}}$ anymore. Moreover, since EMT is employed for solving NFRHT between plates, it fails to accurately capture unique properties of MPs in original grating structures.

The distribution of energy transmission coefficients can effectively predict the radiative heat flux. Consequently, the spectral heat flux is calculated as depicted in Fig. 4. As $\varepsilon_{\text{real}}$ is below 0.1, the spectral heat flux reaches a peak at 2.1×10^{14} rad/s, exceeding 0.6 nJ/(m² rad). However, as $\varepsilon_{\text{real}}$ gradually approaches 1, the heat flux attenuates and the radiative spectrum becomes broader. In other words, when the permittivity of the filled medium approaches zero, it breaks the NFRHT limitation of vacuum-filled gratings and exhibits a remarkable narrow-band characteristic. This is attributed to the fact that the Meta-NP ENZ mode couples MPs and SPPs, and supports the transmission of evanescent waves to large wave vector. Subsequently, with an increase in $\varepsilon_{\text{real}}$, there is a further decrease observed in spectral heat flux. The resonance peaks supported by MPs and SPPs become more distinct, especially with a shift towards lower frequencies for the MPs peak, while the Meta-NP ENZ mode completely disappears. By integrating the spectral heat flux across frequencies, the total heat flux as a function of $\varepsilon_{\text{real}}$ is obtained in Fig. 1(b). The trend of heat-flux curve further confirms the conclusion mentioned in the previous section. Specifically, within the $\varepsilon_{\text{real}}$ range of 0.01–0.1, the total heat flux consistently exceeds 10.1×10^4 W/m² and then sharply decreases. This observation highlights that the NFRHT performance of metamaterials is highly sensitive to variations in $\varepsilon_{\text{real}}$ beyond 0.1.

To visually elucidate the underlying physical mechanism of Meta-NP ENZ mode, we present the distributions of electric field intensity in a period unit at resonance frequencies, as illustrated in Fig. 5. The results are obtained when the plane wave is incident at the resonance frequency using finite-difference time domain. Note that the resonance modes in subpanels are different, with Fig. 5(a) representing the Meta-NP ENZ mode, Fig. 5(b) representing the transition mode

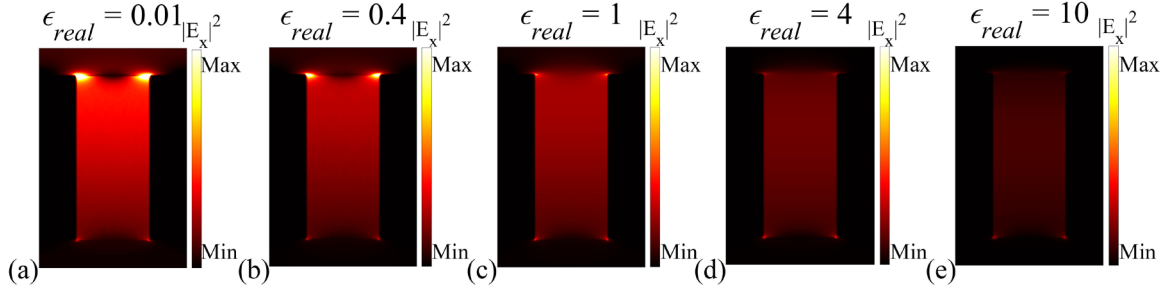


FIG. 5. Distributions of electric field of different ϵ_{real} at the resonance frequencies. (a) $\epsilon_{\text{real}} = 0.01$, $\omega = 2.1 \times 10^{14}$ rad/s; (b) $\epsilon_{\text{real}} = 0.4$, $\omega = 1.98 \times 10^{14}$ rad/s; (c) $\epsilon_{\text{real}} = 1$, $\omega = 1.51 \times 10^{14}$ rad/s; (d) $\epsilon_{\text{real}} = 4$, $\omega = 1.02 \times 10^{14}$ rad/s; and (e) $\epsilon_{\text{real}} = 10$, $\omega = 0.67 \times 10^{14}$ rad/s.

where Meta-NP ENZ mode splits into MPs, and Figs. 5(c)–5(e) representing the MPs mode. We employ a periodic boundary condition in the x direction and a perfectly matched layer in the z direction. It is evident from the figure that when the groove is filled with a nonpolar dielectric, the field intensity enhancement is mainly confined inside the medium. Correspondingly, the electric field inside the Si gratings is extremely weak and negligible. Moreover, as ϵ_{real} increases from 0.01 to 10, there is a gradual attenuation of electric field intensity. Based on these observations and considering continuity conditions,

$$(\mathbf{D}_1 - \mathbf{D}_2) \cdot \hat{\mathbf{n}} = 0, \quad (20)$$

where subscript 1 refers to Si gratings, subscript 2 refers to the nonpolar ENZ dielectric, and $\hat{\mathbf{n}}$ is the boundary unit normal. For lossless medium, Eq. (20) can translate to the following equation:

$$\epsilon_{\text{Si}}(\omega)E_{\text{Si}} = \epsilon_{\text{real}}E_{\text{ENZ}}, \quad (21)$$

where E_i is the component of the electric field of p -polarized wave and ϵ_i is the permittivity. According to Eq. (21), the presence of ENZ leads to a discontinuity in the electric field component at the interface between gratings and nonpolar ENZ dielectric, resulting in a field intensity enhancement within the ENZ medium. A significant local electric field arises at the junction of ENZ dielectric tip with Si gratings and presents a field leakage mode into vacuum space as shown in Figs. 5(a) and 5(b). This phenomenon is attributed to the amplification of Si gratings SPPs by ENZ dielectric at this frequency. In contrast, Figs. 5(c)–5(e) exhibit the characteristics of MPs in gratings rather than SPPs. Considering our previous establishment that Meta-NP ENZ mode can simultaneously couple both SPPs and MPs at identical frequencies, it is important to note that the impact of ENZ on MPs is particularly significant. Consequently, we will conduct an extensive investigation into the physical mechanism of MPs.

The LC circuits are typically used to predict the resonance frequency of MPs. Figure 6(a) represents the LC circuit of Si gratings within a periodic unit, which includes the effective capacitance of the filled medium and the inductances of Si gratings. Here, C_e is the capacitance, which can also be regarded as the channel between neighboring Si ridges. L_m and

L_k are the parallel ridge surface and kinetic inductances in Si grating, respectively. They are expressed as follows:

$$C_e = c_1 \epsilon_0 \epsilon_{\text{ENZ}} \frac{h}{f L_x} \quad (22)$$

$$L_{m1} = 0.5 \mu_0 \frac{f L_x}{L_y} \quad (23)$$

$$L_{k1} = -\frac{h}{\epsilon_0 \omega^2 L_y \delta} \frac{\epsilon'}{(\epsilon'^2 + \epsilon''^2)}, \quad (24a)$$

$$L_{k2} = -\frac{f L_x}{\epsilon_0 \omega^2 L_y \delta} \frac{\epsilon'}{(\epsilon'^2 + \epsilon''^2)}, \quad (24b)$$

$$L_{k3} = -\frac{(1-f)L_x}{\epsilon_0 \omega^2 L_y \delta} \frac{\epsilon'}{(\epsilon'^2 + \epsilon''^2)}, \quad (24c)$$

where $c_1 = 0.35$ is the correction factor, $\epsilon_0 = 8.85 \times 10^{-12}$ F/m is the permittivity of vacuum, $\mu_0 = 4\pi \times 10^{-7}$ is the permeability of vacuum, L_y is the length of the Si grating in the y direction and can be set to unity for one-dimensional Si grating, and $\delta = c/[\omega \cdot \text{Im}(\epsilon_{\text{Si}}^{0.5})]$ is the penetration depth of the electric field. On the other hand, ϵ' and ϵ'' are the real and imaginary parts of the permittivity of Si, respectively. Note that L_{k1} , L_{k2} , and L_{k3} represent the kinetic inductances of the side surface, groove surface, and upper surface, respectively. Hence, the total impedance Z_{tot} of the circuit can be obtained and expressed as

$$Z_{\text{tot}} = j\omega(2L_{k1} + 2L_{m1} + L_{k2} + L_{k3}) - \frac{j}{\omega C_e}, \quad (25)$$

MPs' resonance condition is that the impedance $Z_{\text{tot}} = 0$ and the resonance frequency is obtained as

$$\omega_{\text{MPs}} = \sqrt{\frac{1}{C_e(2L_{k1} + 2L_{m1} + L_{k2} + L_{k3})}}. \quad (26)$$

Due to the fixed geometrical parameters, the ω_{MPs} are solely influenced by the permittivity of dielectric. By solving Eq. (26), it can precisely predict the MPs frequency at 1.51×10^{14} rad/s when ϵ_{real} is equal to 1, indicating the vacuum-filled gratings. To further explain the mechanism of MPs, Fig. 6(b) illustrates the distribution of magnetic field and induced currents at the frequency of 1.51×10^{14} rad/s. Parallel- and opposite induced currents are generated at the interface between adjacent ridges and vacuum, which is a distinctive characteristic of MPs. This observation aligns well with Fig. 3(e), confirming both the existence of MPs and the

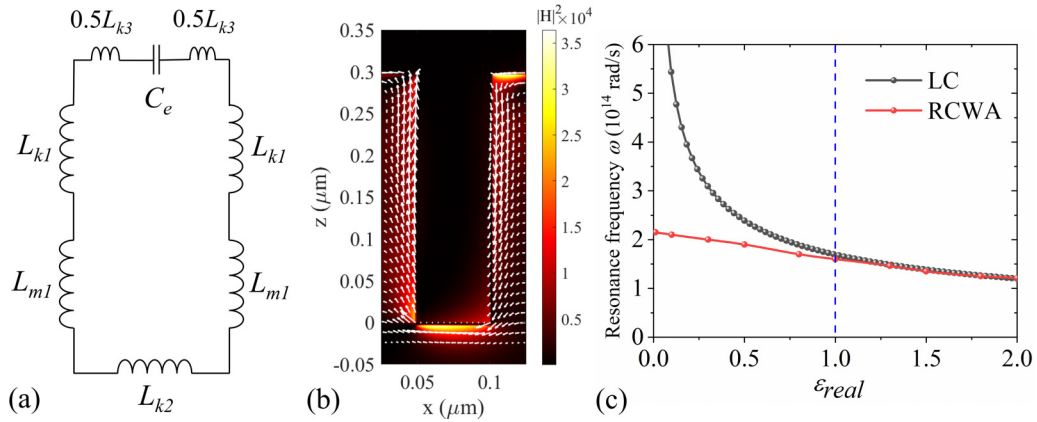


FIG. 6. (a) The configuration of LC circuit in the unit period. (b) Distribution of magnetic field in xz plane, where the white lines indicate the induced current, the arrows indicate the direction, and the lengths indicate the magnitude. (c) Prediction of resonance frequencies by LC circuit compared to RCWA.

accuracy of LC circuit predictions. In addition, we calculate ω_{MPs} as a function of ϵ_{real} by solving Eq. (26) and compare them with the resonance frequencies obtained from the RCWA method as shown in Fig. 6(c). The results predicted by LC circuit precisely coincide with those of the RCWA method only when ϵ_{real} exceeds 1. As ϵ_{real} approaches 0 from 1, the resonance frequencies of LC circuit increase exponentially, while those of RCWA still increase linearly. This implies that the LC circuit is expected to fail when ϵ_{real} is less than 1. This is due to the permittivity of hypothetical nonpolar ENZ dielectric, which is a lossless and nondispersive material, exerting its influence solely on the capacitance C_e in the LC circuit. According to Eq. (22), there exists a linear correlation between C_e and ϵ_{real} , meaning that when permittivity approaches zero, C_e also tends towards zero. As a result, the solutions obtained from solving Eq. (26) increase exponentially. It has been established that as ϵ_{real} is below 1, the MPs are gradually hybridized and eventually get replaced by Meta-NP ENZ mode, where prediction using LC circuit becomes invalid. This perspective can be further verified by geometrical parameter studies.

First, we compare the distribution of energy transmission coefficients of two states with Si grating filling ratios f of 0.2 and 0.8, respectively (the filling ratio in Fig. 3 is 0.5). The grating structure tends to resemble a plate when f approaches 1 under vacuum conditions, resulting in an enhancement of SPPs in Si and an attenuation of MPs in Figs. 7(a) and 7(b). This suggests that the energy transmission coefficients of MPs decay towards lower wave vectors. However, changes in f do not cause any frequency shift for MPs. According to LC circuit prediction, f has a weak influence on frequency shift. When Si gratings are filled with nonpolar ENZ dielectric, SPPs and MPs can hybridize to form Meta-NP ENZ mode at any value of f in Figs. 7(c) and 7(d), demonstrating the robustness of this mode with respect to the filling ratio.

In addition, we compare the distribution of energy transmission coefficients of two states with Si grating height h of 0.1 and 0.5 μm , respectively (the height in Fig. 3 is 0.3 μm). When the filling medium is a vacuum, the MPs' frequency shifts towards lower frequencies with increasing h , which can be accurately predicted using LC circuit in Figs. 7(e) and

7(f). In contrast, the SPPs' frequency remains unaffected as h changes. When h is 0.1 μm , the MPs' frequency approaches to the SPPs frequency, facilitating hybridization of both modes. However, when the filling medium is nonpolar ENZ dielectric, Meta-NP ENZ mode can still be formed at any h by coupling the MPs with SPPs, which extends to larger wave vectors than that in Fig. 7(e) and exhibits superior performance as shown in Figs. 7(g) and 7(h). It should be noted that the superiority of Meta-NP ENZ mode becomes more prominent at higher heights where its resonance frequency always lies between MPs' and SPPs' frequencies. This implies that similar to MPs' frequency, there is a redshift occurring with increasing height for Meta-NP ENZ mode.

Although we can adjust the geometrical parameters to achieve a close frequency match between MPs and SPPs, the coupling effect remains inferior compared to Meta-NP ENZ mode. First, tuning the geometrical parameters is severely limited by the intrinsic frequency of SPPs, meaning that the grating size can only be designed near a fixed frequency. However, the Meta-NP ENZ mode not only enables tuning of MPs' frequency towards higher frequencies but also facilitates tuning of SPPs' frequency towards lower frequencies, ultimately resulting in a unified resonant mode. This makes the grating size independent of SPPs' frequency and allows for significant enhancement of NFRHT simply by reducing permittivity of filling nonpolar dielectric. Such flexibility can not be achieved solely through changes in geometrical parameters. Compared to hybridization of MPs and SPPs by reducing height, the Meta-NP ENZ mode requires not only achieving hybridization of modes but also further enhancing this effect. This amplification surpasses limitations imposed by large-size gratings as well. Therefore, the Meta-NP ENZ mode represents a versatile mode that significantly enhances NFRHT in any gratings while remaining independent from geometrical parameters.

Previously, we have demonstrated the impact of nonpolar ENZ dielectric with ϵ_{real} approaching zero on NFRHT and established the existence of Meta-NP ENZ mode. However, it is essential to note that this conclusion relies on the assumption that the ENZ dielectric is lossless, i.e., the ϵ_{imag} also approaches zero. In far-field radiation, the presence of

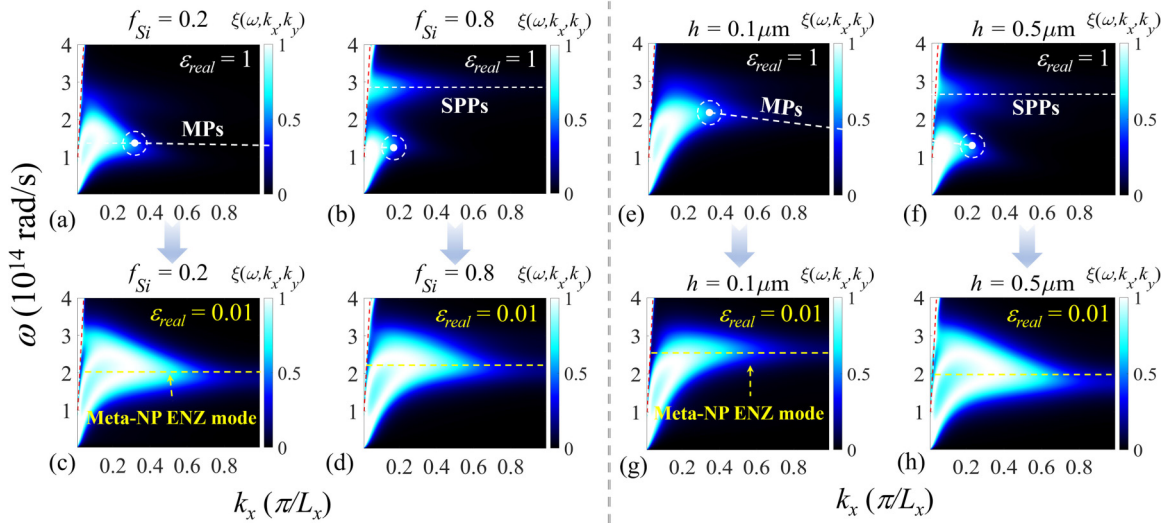


FIG. 7. Contour plots of energy transmission coefficients ξ as the function of Si grating filling ratio f (a)–(d) and height h (e)–(h) at $k_y = 0$. (a) $f_{\text{Si}} = 0.2$, $\epsilon_{\text{real}} = 1$; (b) $f_{\text{Si}} = 0.8$, $\epsilon_{\text{real}} = 1$; (c) $f_{\text{Si}} = 0.2$, $\epsilon_{\text{real}} = 0.01$; (d) $f_{\text{Si}} = 0.8$, $\epsilon_{\text{real}} = 0.01$; (e) $h = 0.1 \mu\text{m}$, $\epsilon_{\text{real}} = 1$; (f) $h = 0.5 \mu\text{m}$, $\epsilon_{\text{real}} = 1$; (g) $h = 0.1 \mu\text{m}$, $\epsilon_{\text{real}} = 0.01$; and (h) $h = 0.5 \mu\text{m}$, $\epsilon_{\text{real}} = 0.01$.

loss poses an inevitable challenge, obscuring various intriguing phenomena such as optical superlensing and topological protection [44–46].

We analyze the distribution of energy transmission coefficients by varying ϵ_{imag} from 0.0001 to 2, as illustrated in Fig. 8. In this paper, we consider three scenarios: when ϵ_{imag} is less than 0.1, the distribution of energy transmission coefficients remains largely unchanged and consistently exhibits characteristics of Meta-NP ENZ mode. They extend towards large wave vectors, and increasing ϵ_{imag} has negligible effect, as shown in Figs. 8(a)–8(c). The resonance peak gradually becomes broader and less sharp within the range of 0.1–1, which is not sustainable at large wave vectors. The distribution becomes flatter compared to Fig. 8(a) when ϵ_{imag} exceeds 1, and the resonance peak shifts towards higher

frequencies. This indicates that an increase in ϵ_{imag} significantly inhibits the formation of Meta-NP ENZ mode, thereby highlighting its sensitivity to the imaginary part. This conclusion is further supported by integrating spectral radiative heat flux. Figure 9(a) illustrates that the spectral heat flux exceeds $0.55 \text{ nJ}/(\text{m}^2 \text{ rad})$ in a narrow band of $2.0 - 2.6 \times 10^{14} \text{ rad/s}$ as ϵ_{imag} is below 0.01. It can be observed that the Meta-NP ENZ mode is not affected by ϵ_{imag} in this range. However, when ϵ_{imag} is above 0.01, the radiative heat flux in the low-frequency range is significantly enhanced, resulting in a broadening of the radiation spectrum.

The spectral range in which the value exceeds $0.55 \text{ nJ}/(\text{m}^2 \text{ rad})$ is $1.4 - 2.7 \times 10^{14} \text{ rad/s}$ when ϵ_{imag} is equal to 0.7. The trend of total radiative heat flux with ϵ_{imag} can be intuitively determined from Fig. 9(b). It is not necessarily true that a

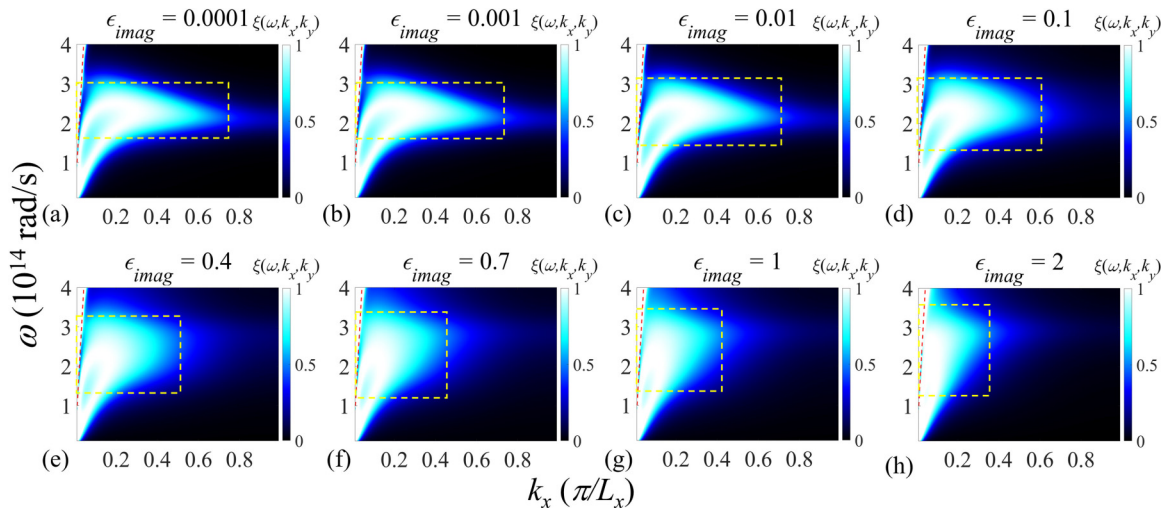


FIG. 8. Contour plots of energy transmission coefficients ξ of different ϵ_{imag} within the first Brillouin zone at $k_y = 0$, and the real part is fixed as 0.01. (a) $\epsilon_{\text{imag}} = 0.0001$, (b) $\epsilon_{\text{imag}} = 0.001$, (c) $\epsilon_{\text{imag}} = 0.01$, (d) $\epsilon_{\text{imag}} = 0.1$, (e) $\epsilon_{\text{imag}} = 0.4$, (f) $\epsilon_{\text{imag}} = 0.7$, (g) $\epsilon_{\text{imag}} = 1$, and (h) $\epsilon_{\text{imag}} = 2$. The dashed rectangular box plots the range of frequencies and wave vectors where the resonance mode are located, which correspond to the range of spectral heat flux greater than $0.35 \text{ nJ}/(\text{m}^2 \text{ rad})$.

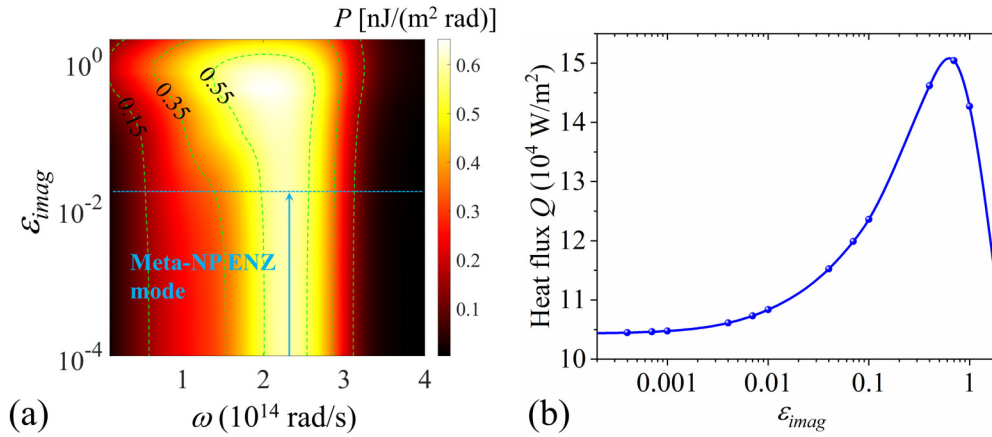


FIG. 9. (a) Contour plot of spectral heat flux as a function of ϵ_{imag} , and the real part is fixed as 0.01. The ϵ_{imag} range of Meta-NP ENZ mode is from 0.0001 to 0.01. (b) Total heat flux as a function of ϵ_{imag} .

closer proximity of ϵ_{imag} to zero may result in a higher heat flux. Instead, there exists a point of maximum value beyond which the heat flux drops dramatically. The increase in the imaginary part leads to a loss of ENZ material, thereby causing the Meta-NP ENZ mode to be less prominent. Despite broadening the radiative spectrum, this also causes the energy transmission coefficients to recede towards small wave vectors and eventually flatten out. In other words, this amplification of radiative heat flux represents a mutation occurring during a transitional phase, which broadens the radiation spectrum while simultaneously maintaining energy transmission coefficients at large wave vectors.

Thus, the increase in ϵ_{imag} suppresses the Meta-NP ENZ mode, aligning with an unfavorable finding in far-field radiation regarding the loss of ENZ materials. However, this increase does not lead to a monotonically decreasing radiative heat flux, suggesting that an increase in losses within a reasonable range can paradoxically improve the performance of ENZ materials. Therefore, ϵ_{imag} does not need to be as close to zero as ϵ_{real} to achieve the peak heat flux, and its role in broadening the radiation spectrum should not be underestimated.

The loss of material can be determined from the divergence of the Poynting vector, which eventually takes the following form:

$$P = 0.5\omega\epsilon_{\text{imag}}|E_{\text{ENZ}}|^2. \quad (27)$$

Thus, the distributions of losses for different ϵ_{imag} are calculated as shown in Fig. 10. It is clear that as ϵ_{imag} approaches zero, the loss of nonpolar ENZ dielectric decreases, which can be directly explained by Eq. (27). It should be noted that $|E_{\text{ENZ}}|^2$ represents the field intensity enhancement that occurs inside the ENZ dielectric due to the Meta-NP ENZ mode. The result obtained from Eq. (21) appears to be directly substituted into Eq. (27), but this assumption holds true only when the dielectric is lossless. In case of a lossy dielectric, the electric field can be expressed as

$$E_{\text{ENZ}} = \frac{\epsilon_{\text{Si}}(\omega)}{[0.01 + i\epsilon_{\text{imag}}]} E_{\text{Si}}. \quad (28)$$

This suggests that the electric field intensity no longer approaches infinite because of losses, even if ϵ_{real} is close to zero. Consequently, E_{ENZ} reduction is the main reason for the suppression of Meta-NP ENZ mode. Thus, the loss of ENZ material presents a problem for near-field radiation as well as restricts far-field radiation, and its impact on the Meta-NP ENZ mode cannot be disregarded.

We have demonstrated that the real and imaginary components of permittivity near zero significantly enhance the NFRHT, respectively. Specifically, our proposed Meta-NP ENZ mode not only overcomes the limitations of Si grating performance but also enables effective utilization of nonpolar ENZ materials in near-field radiation. However, further discussion is required to determine whether this property is

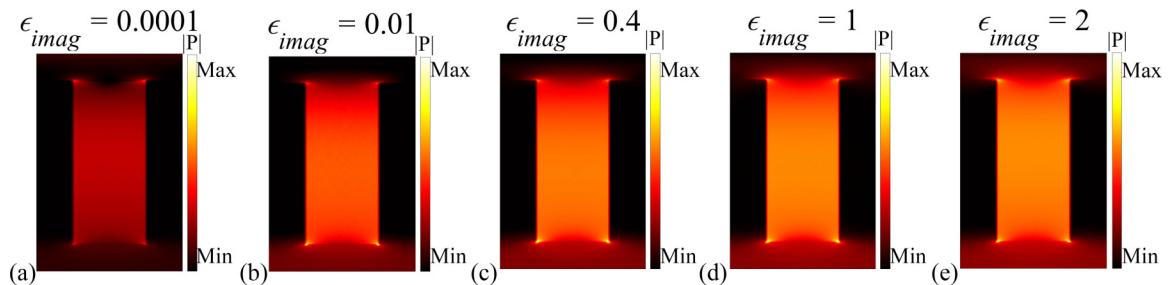


FIG. 10. Distributions of losses of different ϵ_{imag} at the resonance frequencies. (a) $\epsilon_{\text{imag}} = 0.0001$, $\omega = 2.1 \times 10^{14}$ rad/s; (b) $\epsilon_{\text{imag}} = 0.01$, $\omega = 2.21 \times 10^{14}$ rad/s; (c) $\epsilon = 0.4$, $\omega = 2.5 \times 10^{14}$ rad/s; (d) $\epsilon_{\text{imag}} = 1$, $\omega = 2.85 \times 10^{14}$ rad/s; and (e) $\epsilon_{\text{imag}} = 10$, $\omega = 2.98 \times 10^{14}$ rad/s.

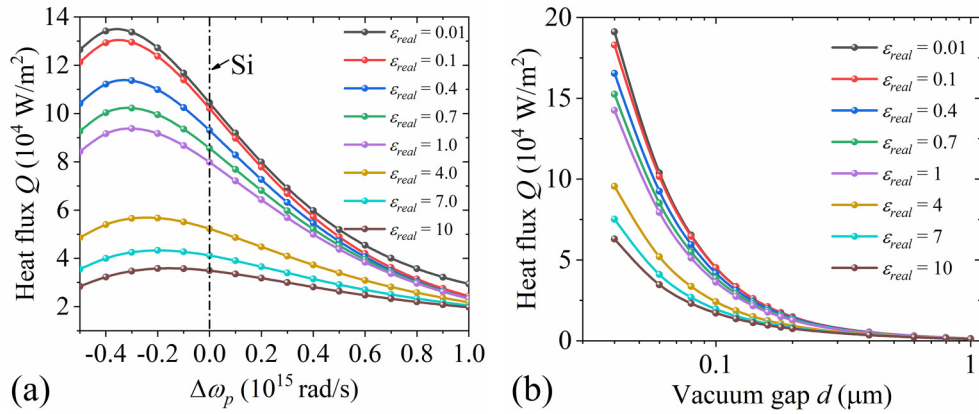


FIG. 11. (a) Total heat flux as a function of $\Delta\omega_p$. (b) Total heat flux vs vacuum gap d from 0.04 to 1 μm . The temperatures of emitter and receiver are fixed as $T_1 = 400$ K and $T_2 = 300$ K in all cases.

exclusive to Si gratings. Therefore, we employ a parametric study in which we artificially introduced a frequency shift $\Delta\omega_p$ for the plasma frequency of Si in Drude model to investigate whether the amplification of radiative heat flux by nonpolar ENZ dielectric is robust with respect to grating materials.

Considering the ω_p of Si mentioned in Sec. II is 1.08×10^{15} rad/s, we explore the range of $\Delta\omega_p$ from -0.5×10^{15} to 1.0×10^{15} rad/s, and the results are shown in Fig. 11(a). Overall, it can be observed that the total radiative heat flux consistently reaches its maximum value at $\varepsilon_{\text{real}} = 0.01$, meaning the robustness of nonpolar ENZ dielectric-induced enhancement with respect to $\Delta\omega_p$. However, this amplification is not sustained. When $\Delta\omega_p$ is negative, the heat flux generally surpasses that in the Si case, and there exists a significant disparity in flux at different $\varepsilon_{\text{real}}$. At $\Delta\omega_p$ is equal to -0.4×10^{15} rad/s, the maximum value exceeds by four times compared to the minimum value. However, when $\Delta\omega_p$ becomes positive, the heat flux exhibits a monotonically decreasing trend with a corresponding decrease in flux disparity. At $\Delta\omega_p$ is equal to 1.0×10^{15} rad/s, the maximum value is only about 1.5 times larger than its minimum value. This is because the permittivity of ENZ dielectric does not have dispersion property, and only the modification in plasma frequency can lead to a frequency shift of Meta-NP ENZ mode. When $\Delta\omega_p$ is negative, as the resonance frequency approaches the characteristic wavelength of thermal radiation, there is an increase in heat flux, resulting in significant variations at lower-frequency bands due to integration. Conversely, when $\Delta\omega_p$ exceeds zero, both the resonance frequencies of Meta-NP ENZ mode and SPPs-MPs blueshift. Despite maintaining its advantage in terms of Meta-NP ENZ mode, the radiative energy transfer becomes naturally less intense in the high-frequency band due to limitations imposed by Eq. (2), thereby reducing disparity in values.

Finally, we compare the total radiative heat flux as a function of vacuum gap d under different $\varepsilon_{\text{real}}$, as shown in Fig. 11(b). The value decreases exponentially with the increasing d and remains its most outstanding performance when $\varepsilon_{\text{real}}$ is equal to 0.01. Notably, the heat flux of nonpolar ENZ dielectric-filled grating diminishes at a significantly faster rate compared to its normal dielectric-filled

counterpart, indicating the rapid decay of Meta-NP ENZ mode and its sensitivity to vacuum gap. When d exceeds 0.4 μm , there is virtually no disparity in radiative heat flux across various $\varepsilon_{\text{real}}$ values, just approaching the limitation of blackbody radiation. This observation implies a complete breakdown of Meta-NP ENZ mode beyond near-field radiation.

IV. CONCLUSIONS

In this work, we present an artificial mode called Meta-NP ENZ mode based on the nonpolar ENZ dielectric-filled Si gratings metamaterial to achieve the enhancement of near-field radiative heat flux. The concept of this mode breaks the conventional near-field limitation of nonpolar ENZ dielectric. As the real and imaginary parts of permittivity approach zero, respectively, we reveal the evolution rule of Meta-NP ENZ mode according to the distributions of energy transmission coefficients and electromagnetic fields, demonstrating the robustness of this effect.

It can be confirmed that Meta-NP ENZ mode is a unique mode independent of geometrical parameters that arises from the hybridization of surface plasmon polaritons (SPPs) and magnetic polaritons (MPs). In particular, it cannot be accurately predicted by LC circuit for determining the resonance frequency of MPs under ENZ conditions. Similar to far-field radiation, the nonpolar ENZ dielectric itself does not participate in radiative heat transfer but can create a remarkable field intensity enhancement inside the structure, which is primarily responsible for Meta-NP ENZ mode. On the contrary, the imaginary part near zero does not allow the radiative heat flux to reach maximum value. Although the Meta-NP ENZ mode gradually deteriorates as the imaginary part increases, there exists a transient state within the narrow range from 0.1 to 1, exhibiting an anomalous amplification in heat flux. Furthermore, this enhancement of heat flux is robust with respect to the frequency shift of metal plasma frequency. The applicability of this theory can extend to other types of gratings, enabling the exploration of higher-dimensional and more intricate metamaterials. Our proposed Meta-NP ENZ mode paves the way for an avenue in near-field radiative heat transfer.

ACKNOWLEDGMENTS

This work was supported by the National Natural Science Foundation of China (Grant No. U22A20210), by the Fundamental Research Funds for the Central Universities (Grants

No. FRFCU5710094020 and No. HIT.DZJJ.2023098), and by the Natural Science Foundation of Heilongjiang Province (Grant No. LH2020E046). C.-L.Z. acknowledges the China Scholarship Council (CSC) for financial support (Grant No. 02206120132).

-
- [1] A. Anopchenko, S. Gurung, S. Bej, and W. Howard, Field enhancement of epsilon-near-zero modes in realistic ultrathin absorbing films, *Nanophotonics* **12**, 2913 (2023).
- [2] K. M. Roccapiore, A. Bozhko, G. Nazarikov, V. P. Drachev, and A. Krokhin, Surface plasmon at a metal-dielectric interface with an epsilon-near-zero transition layer, *Phys. Rev. B* **103**, L161404 (2021).
- [3] A. Baev, P. N. Prasad, M. Z. Alam, and R. W. Boyd, Dynamically controlling local field enhancement at an epsilon-near-zero/dielectric interface via nonlinearities of an epsilon-near-zero medium, *Nanophotonics* **9**, 4831 (2020).
- [4] M. A. Vincenti, M. Kamandi, D. de Ceglia, C. Guclu, M. Scalora, and F. Capolino, Second-harmonic generation in longitudinal epsilon-near-zero materials, *Phys. Rev. B* **96**, 045438 (2017).
- [5] D. Polder and M. Van Hove, Theory of radiative heat transfer between closely spaced bodies, *Phys. Rev. B* **4**, 3303 (1971).
- [6] A. I. Volokitin and B. N. J. Persson, Near-field radiative heat transfer and noncontact friction, *Rev. Mod. Phys.* **79**, 1291 (2007).
- [7] T. Kralik, P. Hanzelka, M. Zobac, V. Musilova, T. Fort, and M. Horak, Strong near-field enhancement of radiative heat transfer between metallic surfaces, *Phys. Rev. Lett.* **109**, 224302 (2012).
- [8] C. Lucchesi, Design and development of a near-field thermophotovoltaic conversion device, Ph.D. diss., Université de Lyon, 2020.
- [9] H. Hajian, I. D. Rukhlenko, Veysel Erçağlar, G. W. Hanson, and E. Özbay, Epsilon-near-zero enhancement of near-field radiative heat transfer in BP/HBN and BP/ α -MoO₃ parallel-plate structures, *Appl. Phys. Lett.* **120**, 112204 (2022).
- [10] J. Zhang, H. Liu, N. Zhang, Y. Hu, Y. Sun, and X. Wu, Epsilon-near-zero characteristics of near-field radiative heat transfer between α -MoO₃ slabs, *Phys. Chem. Chem. Phys.* **25**, 1133 (2023).
- [11] J. B. Pendry, Negative refraction makes a perfect lens, *Phys. Rev. Lett.* **85**, 3966 (2000).
- [12] F. Mesa, M. J. Freire, R. Marqués, and J. D. Baena, Three-dimensional superresolution in metamaterial slab lenses: Experiment and theory, *Phys. Rev. B* **72**, 235117 (2005).
- [13] D. Schurig, J. J. Mock, B. J. Justice, S. A. Cummer, J. B. Pendry, A. F. Starr, and D. R. Smith, Metamaterial electromagnetic cloak at microwave frequencies, *Science* **314**, 977 (2006).
- [14] W. Cai, U. K. Chettiar, A. V. Kildishev, and V. M. Shalaev, Optical cloaking with metamaterials, *Nat. Photon.* **1**, 224 (2007).
- [15] J. Li and J. B. Pendry, Hiding under the carpet: A new strategy for cloaking, *Phys. Rev. Lett.* **101**, 203901 (2008).
- [16] M. M. Sigalas and E. N. Economou, Elastic and acoustic wave band structure, *J. Sound Vibr.* **158**, 377 (1992).
- [17] S. A. Cummer, J. Christensen, and A. Alù, Controlling sound with acoustic metamaterials, *Nat. Rev. Mater.* **1**, 16001 (2016).
- [18] J.-P. Groby, N. Jiménez, and V. Romero-García, Acoustic metamaterial absorbers, *Top. Appl. Phys.* **143**, 167 (2021).
- [19] Z. Zheng, A. Wang, and Y. Xuan, Spectral tuning of near-field radiative heat transfer by graphene-covered metasurfaces, *J. Quant. Spectrosc. Radiat. Transf.* **208**, 86 (2018).
- [20] K. Shi, F. Bao, and S. He, Enhanced near-field thermal radiation based on multilayer Graphene-HBN heterostructures, *ACS Photon.* **4**, 971 (2017).
- [21] Y. Taniguchi, K. Isobe, and K. Hanamura, Enhancement of spectrally controlled near-field radiation transfer by magnetic polariton generated by metal-insulator-metal structures, *Appl. Therm. Eng.* **183**, 116041 (2021).
- [22] J.-Y. Chang, Y. Yang, and L. Wang, Enhanced energy transfer by near-field coupling of a nanostructured metamaterial with a graphene-covered plate, *J. Quant. Spectrosc. Radiat. Transf.* **184**, 58 (2016).
- [23] B. Zhao, B. Guizal, Z. M. Zhang, S. Fan, and M. Antezza, Near-field heat transfer between Graphene/HBN multilayers, *Phys. Rev. B* **95**, 245437 (2017).
- [24] G. Xu, J. Sun, H. Mao, and T. Pan, Near-field radiative thermal rectification assisted by black phosphorus sheets, *Int. J. Therm. Sci.* **149**, 106179 (2020).
- [25] J. Dai, S. A. Dyakov, and M. Yan, Radiative heat transfer between two dielectric-filled metal gratings, *Phys. Rev. B* **93**, 155403 (2016).
- [26] G. Bimonte, Scattering approach to Casimir forces and radiative heat transfer for nanostructured surfaces out of thermal equilibrium, *Phys. Rev. A* **80**, 042102 (2009).
- [27] R. Messina and M. Antezza, Scattering-matrix approach to Casimir-Lifshitz force and heat transfer out of thermal equilibrium between arbitrary bodies, *Phys. Rev. A* **84**, 042102 (2011).
- [28] X. Liu, B. Zhao, and Z. M. Zhang, Enhanced near-field thermal radiation and reduced casimir stiction between doped-Si gratings, *Phys. Rev. A* **91**, 062510 (2015).
- [29] V. Fernández-Hurtado, F. J. García-Vidal, S. Fan, and J. C. Cuevas, Enhancing near-field radiative heat transfer with Si-based metasurfaces, *Phys. Rev. Lett.* **118**, 203901 (2017).
- [30] R. Messina, A. Noto, B. Guizal, and M. Antezza, Radiative heat transfer between metallic gratings using Fourier modal method with adaptive spatial resolution, *Phys. Rev. B* **95**, 125404 (2017).
- [31] M. G. Moharam, T. K. Gaylord, E. B. Grann, and D. A. Pommert, Formulation for stable and efficient implementation of the rigorous coupled-wave analysis of binary gratings, *J. Opt. Soc. Am. A* **12**, 1068 (1995).
- [32] X. L. Liu, R. Z. Zhang, and Z. M. Zhang, Near-field radiative heat transfer with doped-silicon nanostructured metamaterials, *Int. J. Heat Mass Transf.* **73**, 389 (2014).
- [33] M. Lobet, N. Kinsey, I. Liberal, H. Çağlayan, P. A. Huidobro, E. Galiffi, J. R. Mejía-Salazar, G. Palermo, Z. Jacob, and

- N. Maccaferri, New horizons in near-zero refractive index photonics and hyperbolic metamaterials, *ACS Photon.* **10**, 3805 (2023).
- [34] K. Z. Shi, F. L. Bao, N. He, and S. L. He, Near-field heat transfer between graphene-Si grating heterostructures with multiple magnetic-polaritons coupling, *Int. J. Heat Mass Transf.* **134**, 1119 (2019).
- [35] B. Zhao, L. Wang, Y. Shuai, and Z. M. Zhang, Thermophotovoltaic emitters based on a two-dimensional grating/thin-film nanostructure, *Int. J. Heat Mass Transf.* **67**, 637 (2013).
- [36] Y. Guo, S. Zhou, B. Xiong, Y. Shuai, and J. Zhao, Mechanism and prediction of multi-mode magnetic polaritons by MCLC circuit model in complex micro/nanostructures, *J. Quant. Spectrosc. Radiat. Transf.* **269**, 107700 (2021).
- [37] L. Wang and Z. M. Zhang, Effect of magnetic polaritons on the radiative properties of double-layer nanoslit arrays, *J. Opt. Soc. Am. B-Opt. Phys.* **27**, 2595 (2010).
- [38] A. Ghanekar, M. Ricci, Y. Tian, O. Gregory, and Y. Zheng, Strain-induced modulation of near-field radiative transfer, *Appl. Phys. Lett.* **112**, 241104 (2018).
- [39] X. L. Liu, T. J. Bright, and Z. M. Zhang, Application conditions of effective medium theory in near-field radiative heat transfer between multilayered metamaterials, *J. Heat Transf.* **136**, 092703 (2014).
- [40] K. Shi, Z. Chen, X. Xu, J. Evans, and S. He, Optimized colossal near-field thermal radiation enabled by manipulating coupled plasmon polariton geometry, *Adv. Mater.* **33**, 2106097 (2021).
- [41] K. Shi, Z. Chen, Y. Xing, J. Yang, X. Xu, J. S. Evans, and S. He, Near-field radiative heat transfer modulation with an ultrahigh dynamic range through mode mismatching, *Nano Lett.* **22**, 7753 (2022).
- [42] W. B. Zhang, C. Y. Zhao, and B. X. Wang, Enhancing near-field heat transfer between composite structures through strongly coupled surface modes, *Phys. Rev. B* **100**, 075425 (2019).
- [43] H. Wu, X. Liu, Y. Cai, L. Cui, and Y. Huang, Near-field radiative heat transfer modulated by nontrivial topological surface states, *Mater. Today Phys.* **27**, 100825 (2022).
- [44] C. J. Zapata-Rodríguez, D. Pastor, Juan José Miret, and S. Vuković, Uniaxial epsilon-near-zero metamaterials: From superlensing to double refraction, *J. Nanophoton.* **8**, 083895 (2014).
- [45] S. S. Kharintsev, A. V. Kharitonov, A. N. Alekseev, and S. G. Kazarian, Superresolution stimulated Raman scattering microscopy using 2-ENZ nano-composites, *Nanoscale* **11**, 7710 (2019).
- [46] S. Jahani, H. Zhao, and Z. Jacob, Switching Purcell effect with nonlinear epsilon-near-zero media, *Appl. Phys. Lett.* **113**, 021103 (2018).